Morphology-controlled Copper Nanowires Synthesis and Magnetic Field Assisted Self-assembly

Srikar Rao Darmakkolla, Mitra Ghobadi, Lester Lampert, Amanda F. Pareira, Ana Jenike, Musa Tahir and Shankar B. Rananavare*

Department of Chemistry, Portland State University, Oregon, USA, 97201.

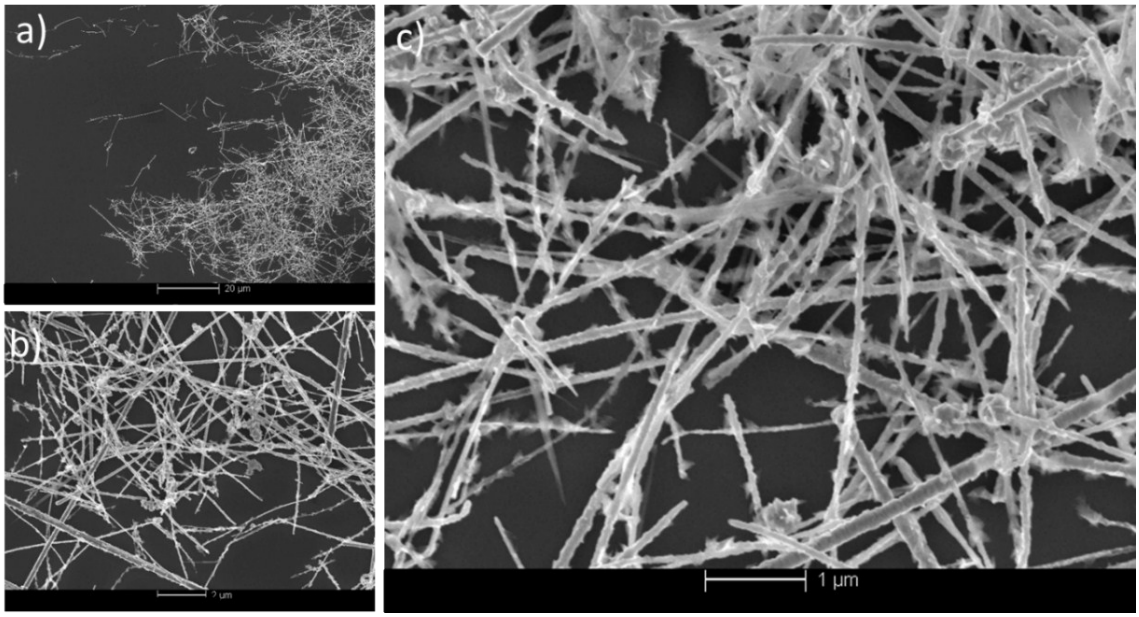

Figure S1. SEM images of Copper Nanowires (Cu NWs) synthesized using $8.28x10^{-3}$ M concentration of hydrazine.

Table S1 Aspect ratios of Cu NWs as a function of synthesis temperature

Temp. (°C)	Average Length (µm)	Average Diameter (nm)	Aspect ratio
60	32 ± 7	160 ± 30	200
70	25 ± 6	170 ±50	147
80	15 ± 4	210 ± 60	71
90	7 ± 2	215 ± 35	32

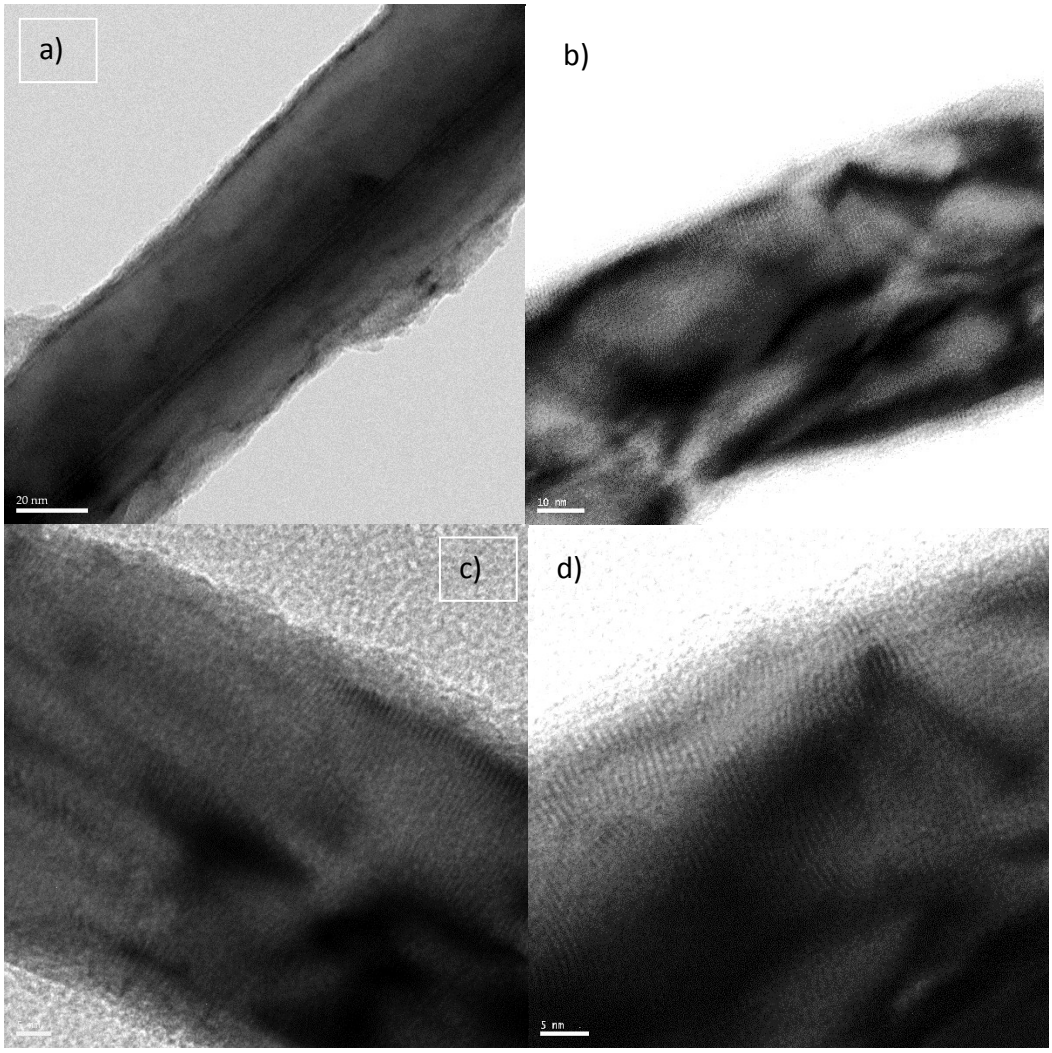

Figure S2. TEM image of Cu NW synthesized using lower 5.73×10^{-3}M concentration of hydrazine highlighting its particle-free and smooth surface a); Higher magnification TEM images b)-d). Scale bar in c) corresponds to 5 nm. Owing to the large NW diameter and polycrystallinity of Cu NWs, we were unable to obtain HR-TEM images.

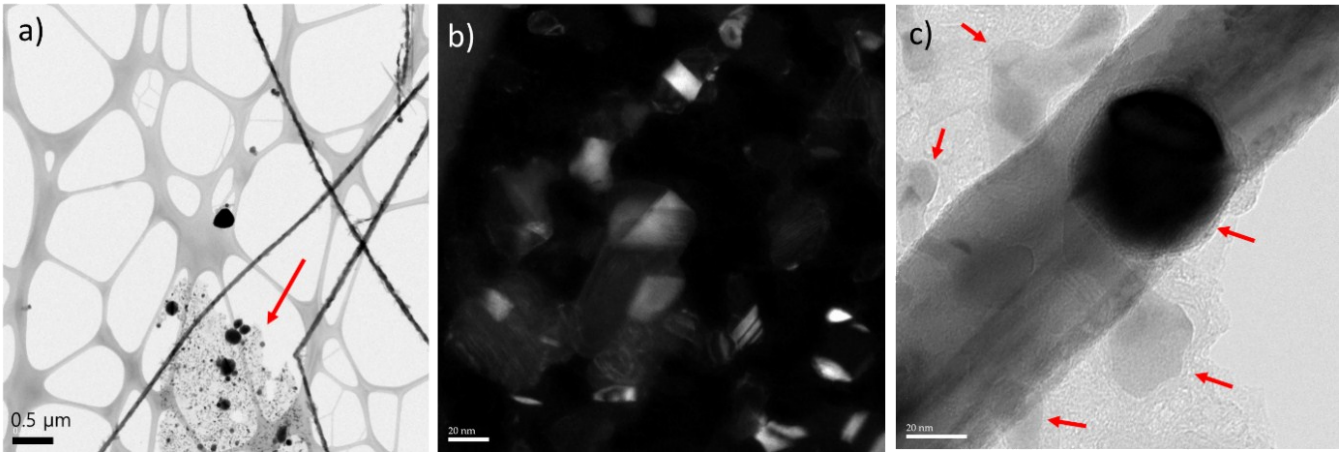

Figure S3. Low magnification bright field a), and high magnification darkfield b), TEM images showing the presence of Cu nanoparticles. Higher magnification bright field images b,c showed nanoparticles bound to the surface of the Cu nanowire at multiple sites (pointed out with arrows).

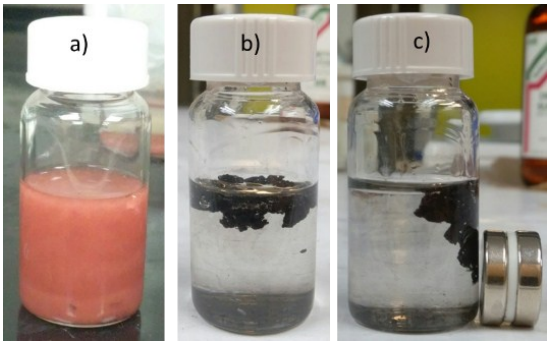

Figure S4. Digital photographs of nickel electroless plating solution before Ni deposition of on Cu-NWs containing a mixture of Cu NWs / $Ni(NO_3)_2$ / Hydrazine in ethylene glycol solvent a). b) Image after heating at 200 °C for 10 minutes revealed floating of dark-colored nickel coated Cu NWs at air-water interface b), an image illustrating attraction of NWs to a Neodymium disc magnet c).

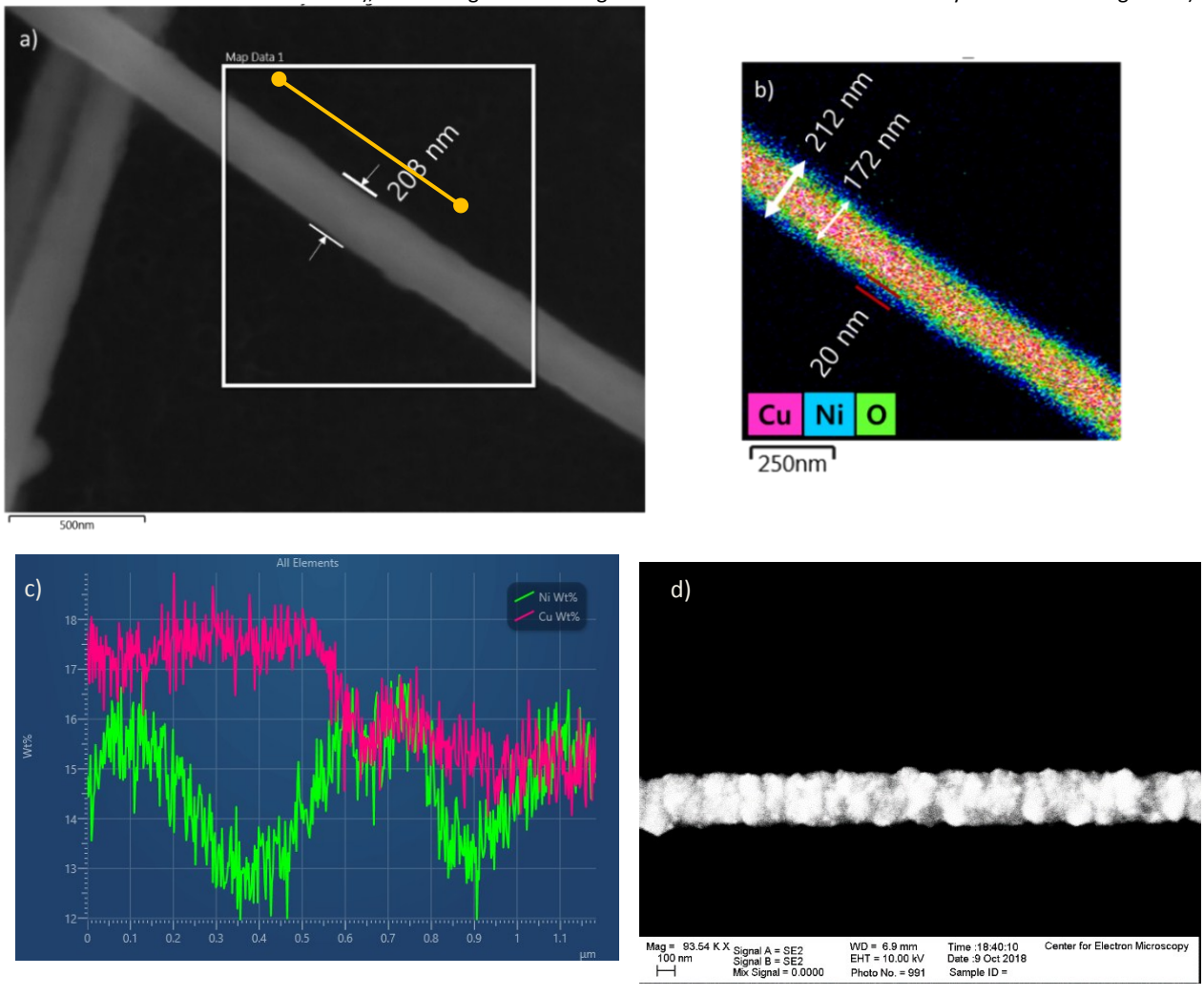

Figure S5. SEM image of nickel coated CuNWs a) and elemental mapping displaying the distribution of copper core and nickel coating on the surface b). Also, noticeable was an oxygen layer between copper and nickel layers possibly be due to surface oxidation of copper while cleaning the as-synthesized Cu-NWs in an aqueous solution. EDX analyzed concentration scan along Cu/NiNW longitudinal

indicates roughly equal Cu and Ni atomic weight percent concentrations with an approximate variation of about 10-15 percent on 1 μm scale c). Equating the volumes of Nickel and copper layers, i.e., $\pi\left(r_1^2 - r_2^2\right)l = \pi r_2^2 l$, (where r_1 and r_2 the radii of core+shell NW and copper NW core respectively, and *l* is the length of NW) yields $r_1 = \sqrt{2}\, r_2$, Thus, Taking into account $r_1 \approx 100\ nm$, the *predicted* Nickel shell thickness is: $r_1 - r_2 = r_1\left[1 - \frac{1}{\sqrt{2}}\right] \approx 26\ nm$, in rough agreement with data shown in b). High magnification SEM image of Cu/Ni NW showing the surface roughness of ≈ 10-15 nm d).

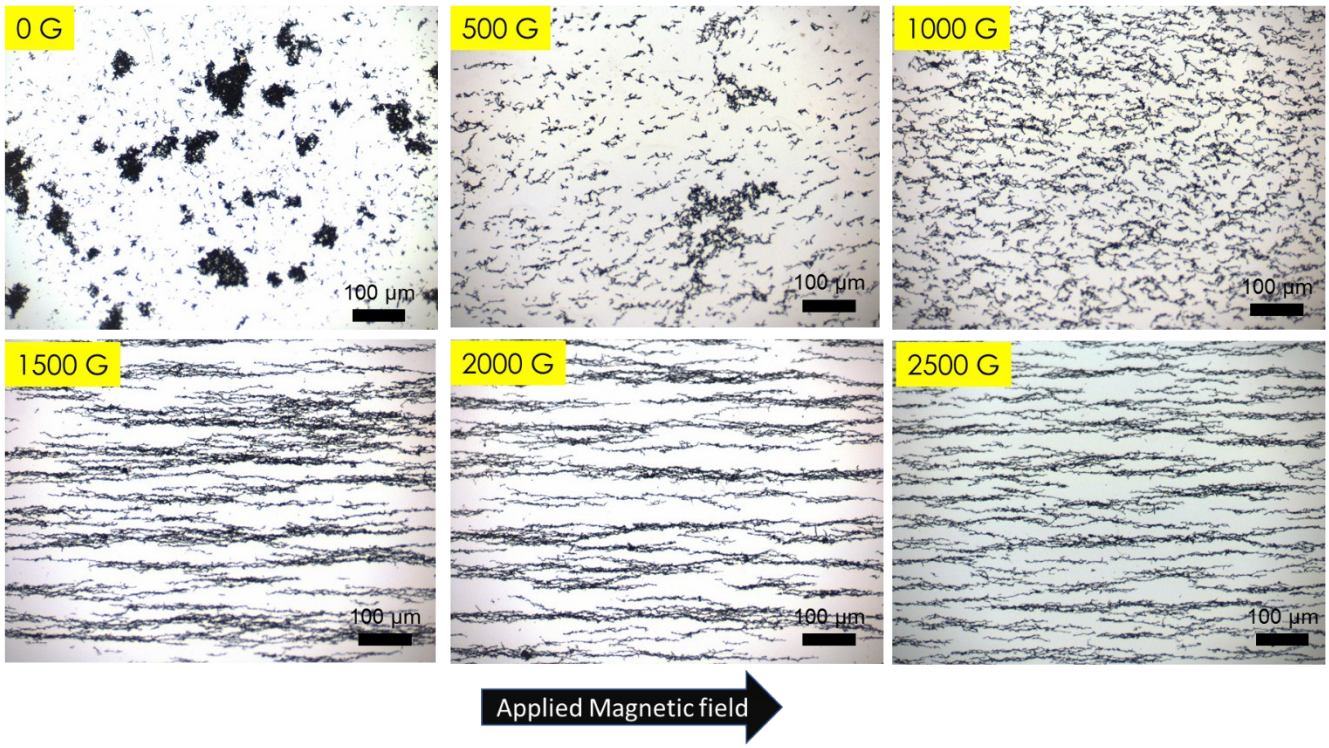

Figure S6. Reflectance optical micrographs of the alignment stages of Cu/Ni NWs during evaporation as the applied magnetic field varied from 0 Gauss to 2500 Gauss. Note the increase in the length of NW chains with an increase in magnetic field strength. The concentration of nanowires in the depositing suspension was 0.5 mg/mL, and the substrate was a silicon wafer.

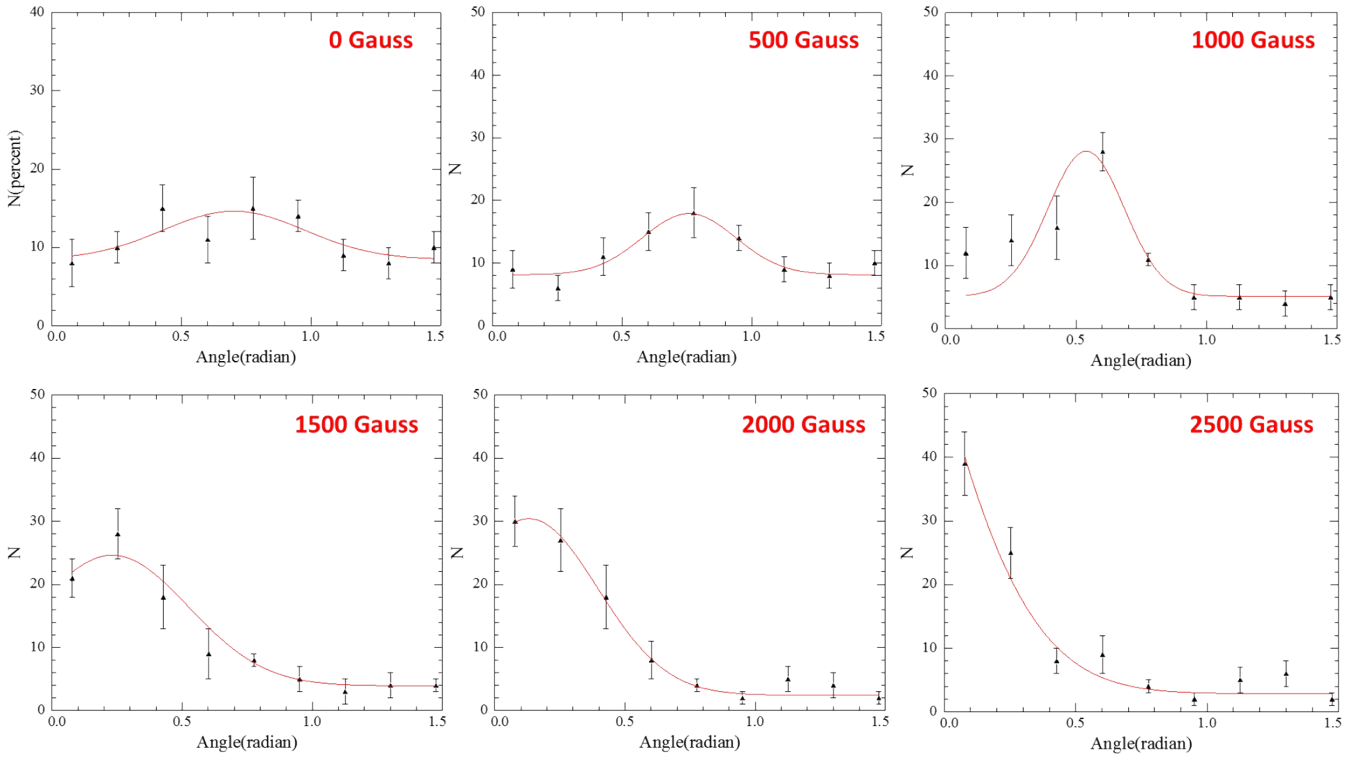

Figure S7. Several (>250 NWs) isolated Cu/Ni NWs, were analyzed to extract an alignment histogram using Image J software freely available at NIH website. Continuous red lines indicate the best-fit line through the Cu/Ni NWs alignment histogram to a Gaussian distribution at the applied magnetic field strengths, as indicated.

$$N(\theta) = Ae^{-\left(\frac{(\theta-<\theta>)}{\Delta\theta}\right)^2} + B$$

A and *B* are normalization constant and constant background fitting parameters, respectively. *N(ϑ)* is a number of nanowires oriented at angle θ in a bin size of 0.2 radians. <*ϑ*> and *Δϑ* are the average absolute value of the NW orientational angle and the width of the distribution respectively. The best-fit parameters and respective curve fitting uncertainties appear in **Table S2.**

Table S2: Field dependent mean Cu/Ni NW alignment angle and its width of the distribution.

Field Strength(Gauss)	<θ>(radian)	Δθ (radian)
000	0.7±0.1	0.4±0.2
500	0.75±0.05	0.25±0.08
1000	0.54±0.03	0.21±0.03
1500	0.23±0.07	0.41±0.08
2000	0.13±0.09	0.37±0.09
2500	0.3±0.7	0.5±0.3

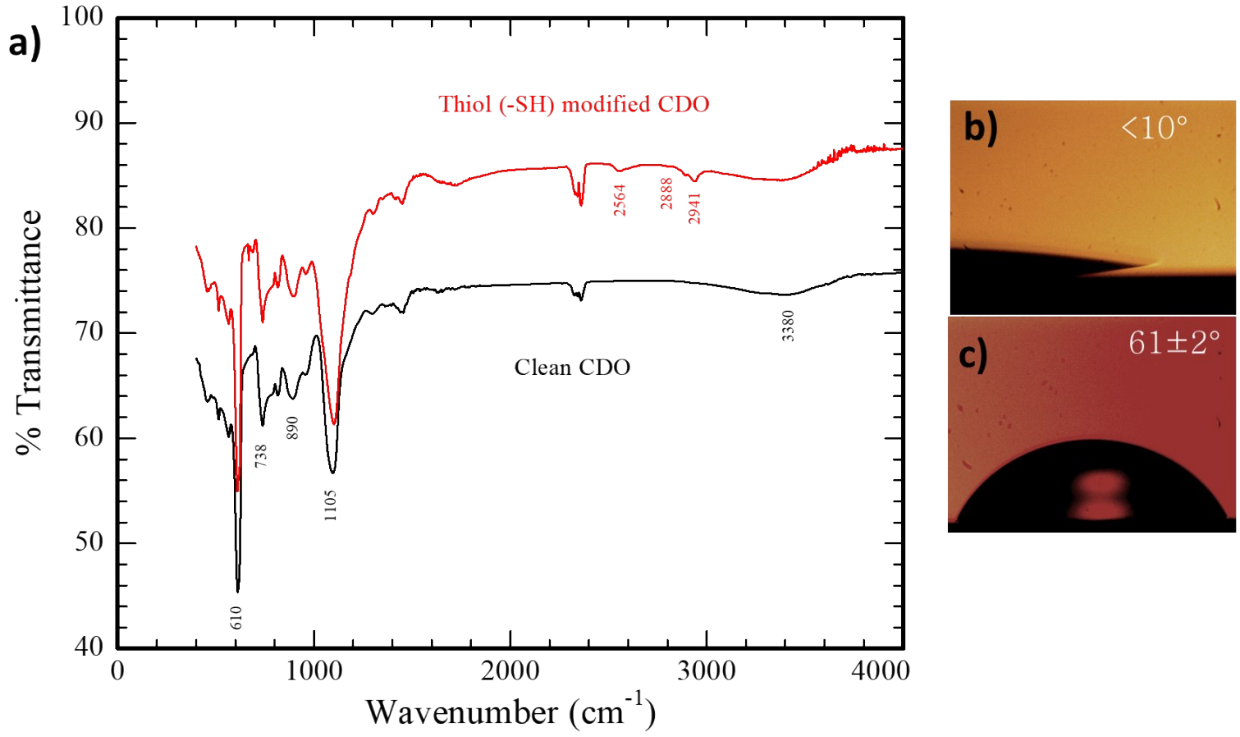

Figure S8. FTIR spectra of clean CDO (black line) and thiol (-SH) functionalized (red line) CDO a). Water drop shapes before and after derivatization b) and c). Estimated contact angle measurement from these images revealed surface hydrophilicity change of clean CDO b), and after thiol (-SH) functionalization c). FTIR spectra, and water contact angles before (control) and after thiol (-SH) functionalized were in good agreement with the literature reported data [1-3].

Ultrasonication of deposited Cu/Ni NWs on CDO surface provided a qualitative measure of their binding strength. The test involved deposition of Cu/Ni NWs aqueous suspension on a clean (control) and thiol-derivatized CDO surfaces followed by drying. The NW laden CDO wafers were immersed in an ethanol solvent in an ultrasonicator (Ultrasonicator, Chicago Electric Power Tools, 2.5 L capacity and operating at 42 kHz frequency). In less than four seconds of ultrasonication, the majority of the NWs were removed from the clean CDO substrate, whereas, the thiol-functionalized surface held the NWs up to 30 seconds without significant detachment.

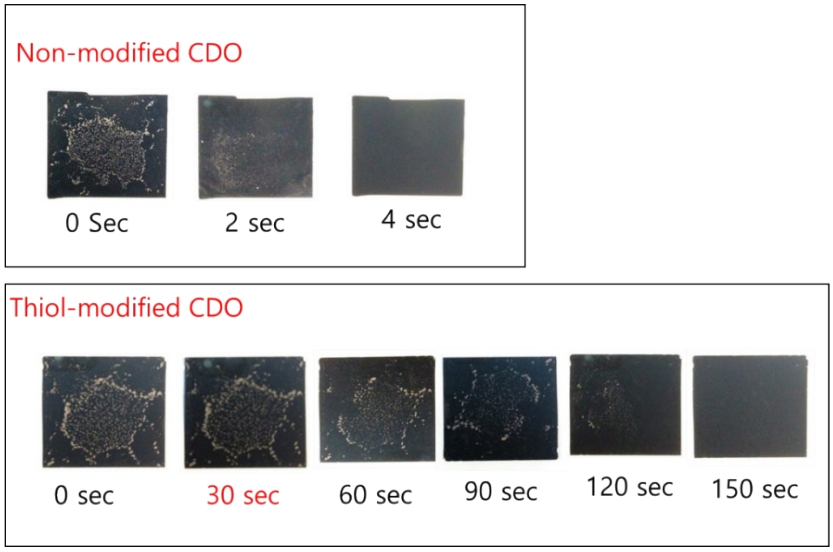

Digital image of ultra sonication system.
(CHICAGO Electric Power tools, 2.5 L, 120v, 160w, 42 kHz frequency)

Figure S9. Digital photographs of NW deposits illustrating the adhesion strength of Cu/Ni NWs on to the clean CDO and thiol (-SH) functionalized CDO substrate A photograph of ultra-sonication setup for testing adhesion strength of NWs to CDO substrates in an ethanol solvent. For thiol functionalized surface, up to 30 secs of sonication, no significant loss of NWs from the CDO surface was noticed.

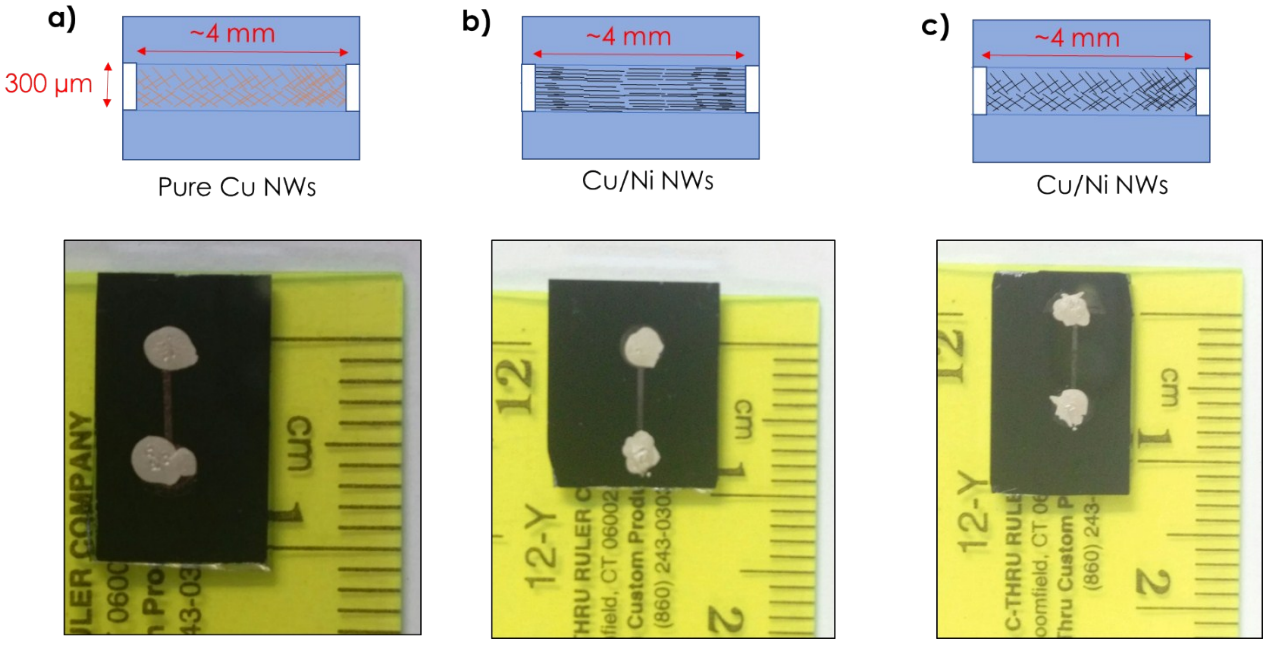

Figure S10. Schematic diagrams and digital photographs showing interconnect channels fabricated using different types and alignment of NWs. The random orientation of Cu NWs a), unidirectionally aligned Cu/Ni NWs b), and randomly oriented Cu/Ni NWs c) respectively.

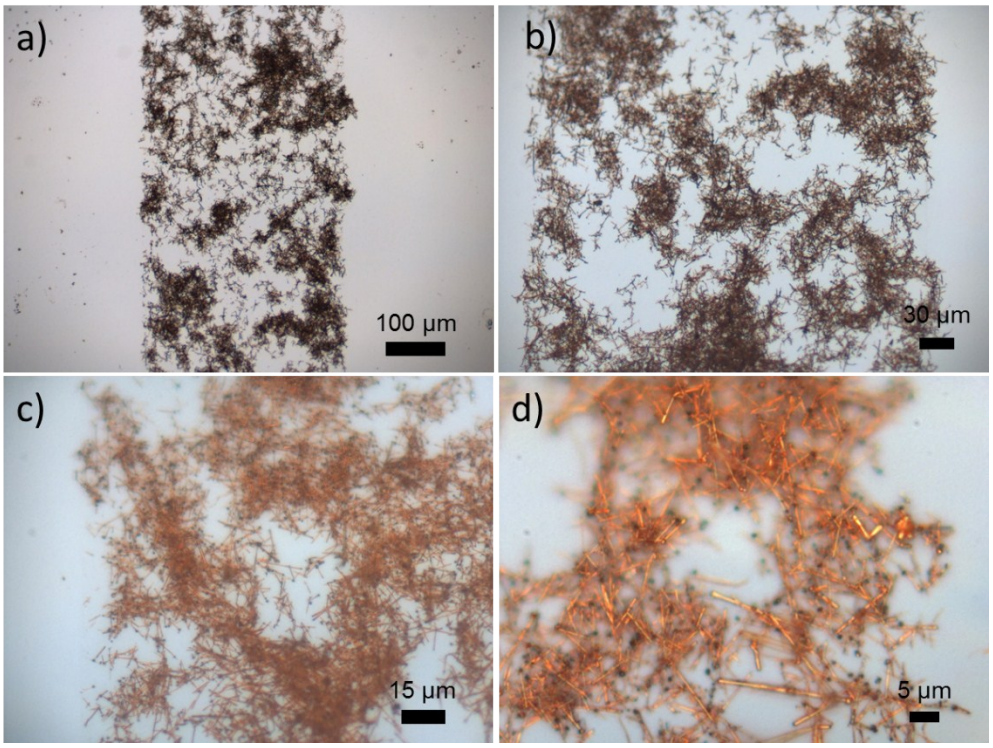

Figure S11. Optical micrographs of Cu NWs deposited in a channel at various magnification scales showing the randomly oriented Cu NWs.

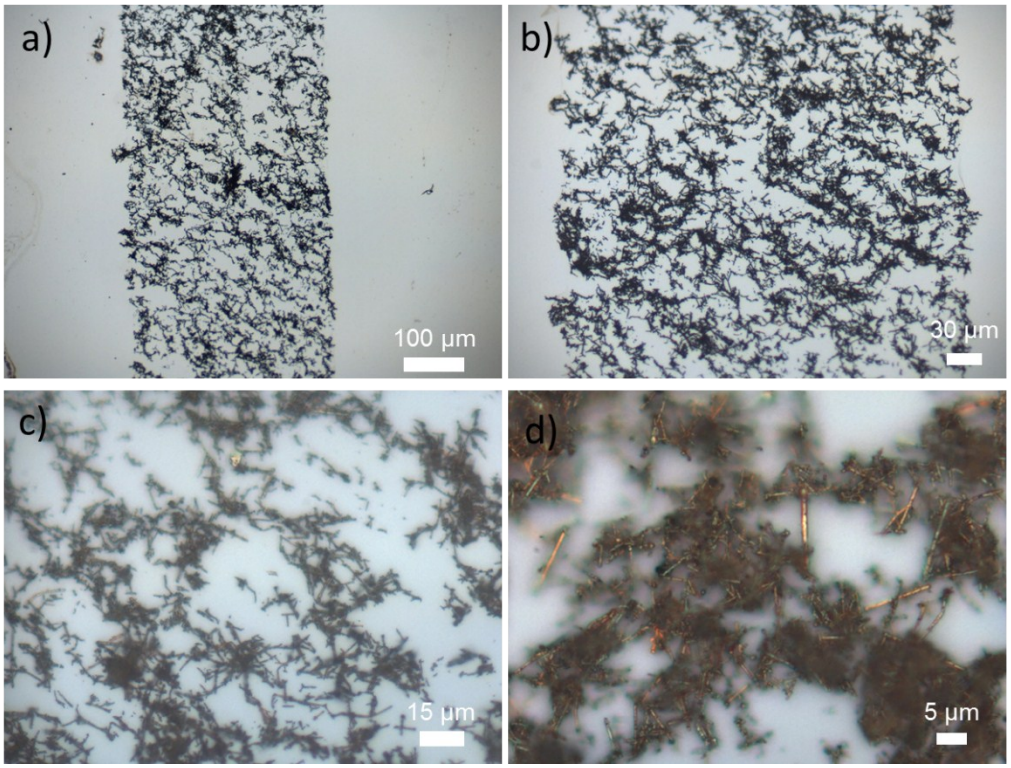

Figure S12. Optical micrographs of Cu/Ni NWs deposited in a channel at various magnification scales showing randomly oriented NWs in the absence of an external magnetic field.

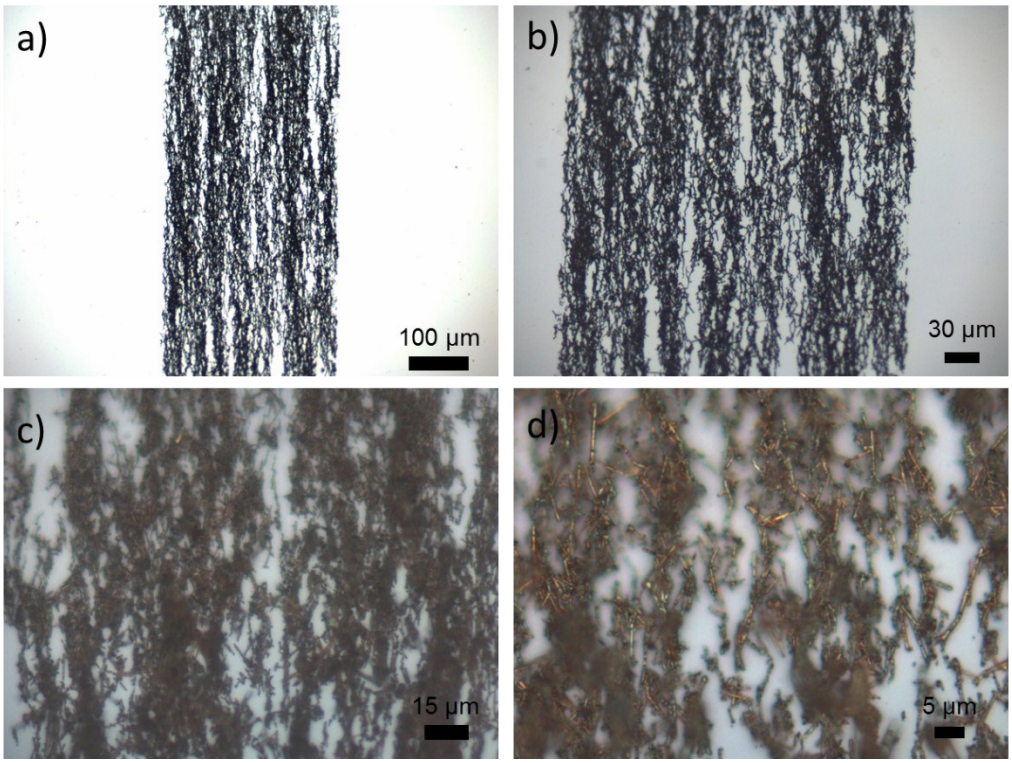

Figure S13. Optical micrographs of Cu/Ni NWs deposited in a lithographically patterned channel at various magnification scales showing directionally oriented NWs in the presence of magnetic field strength of 2500 Gauss.

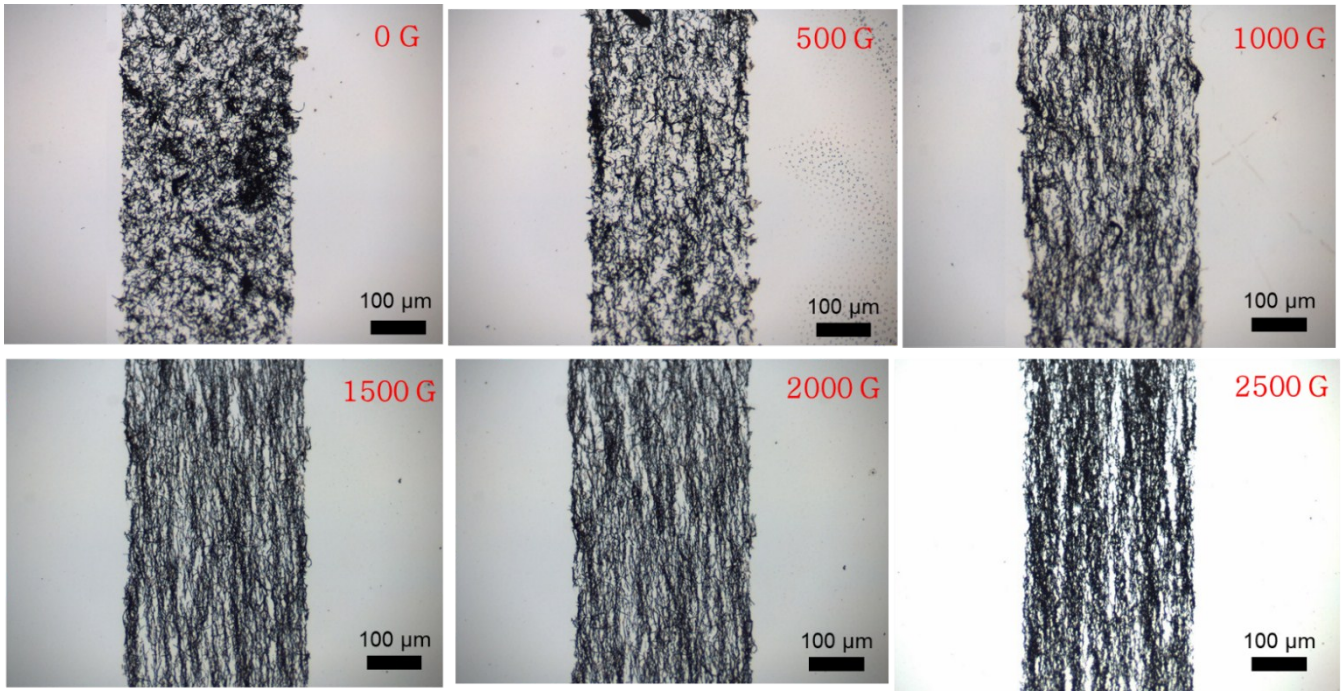

Figure S14. Optical images of Cu/Ni NWs deposited in a lithographically patterned channel in applied magnetic field strength varying from 0 to 2500 Gauss.

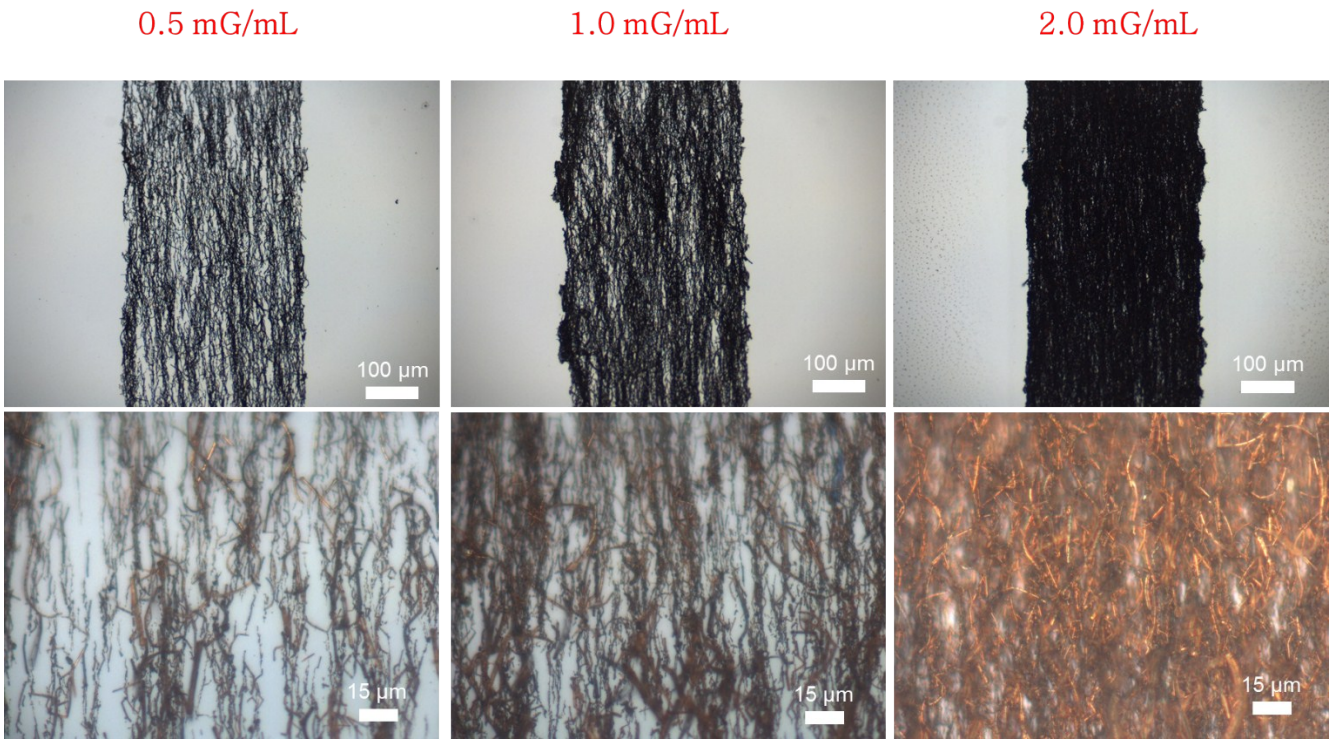

Figure S15. Low and high magnification optical micrographs showing the effect of NW concentration of 0.5 mg/mL, 1.0 mg/mL, and 2 mg/mL respectively, aligned with a magnetic field strength of 2500 Gauss. Note these longer nanowires tend to bend when magnetized.

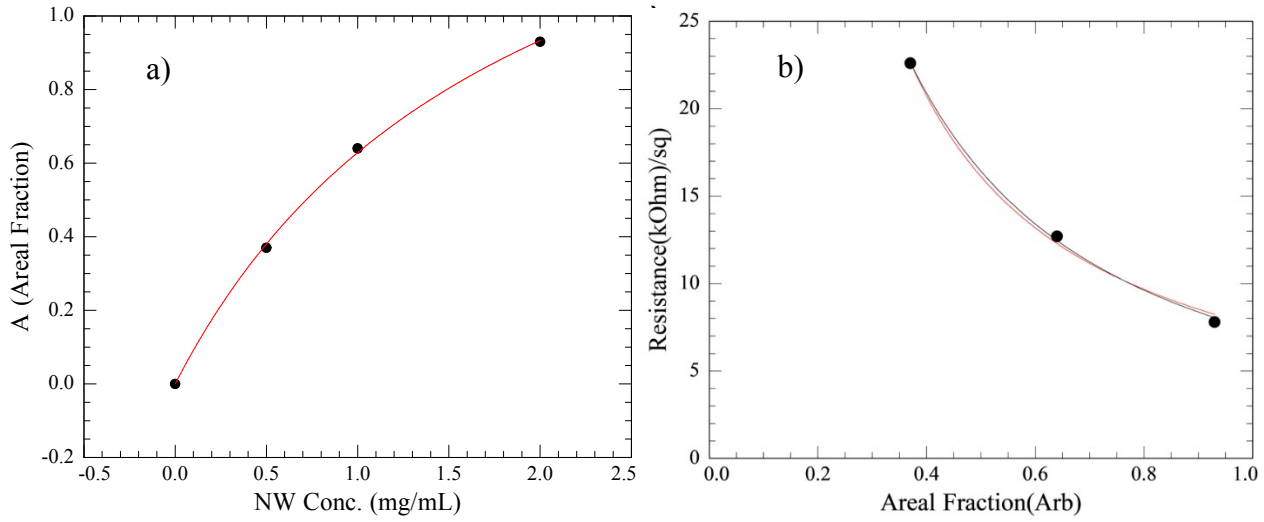

Figure S16. The areal fraction of the NWs channel was calculated in an automatic threshold analysis method (Lever's rule) using an Image-J application (Freeware available from NIH). The NW areal fraction data were fitted to a Langmuir type model with respect to the concentration of NWs (i.e., $A \approx a.C/(1+b.C)$ where C is the NW concentration in depositing solution. The best-fit values of *a* and *b* were 0.96 ± 0.04, 0.53 ± 0.05 a). The sheet resistance of well-aligned Cu/Ni NWs as a function of the areal fraction for NW deposits generated by 0.5, 1.0 and 2.0 mg/mL NW concentration. The percolation model of conductivity was used to fit the data with following fitting equation $R(k\Omega) = 6.7\ (A-0.08)^{-1.0}$, with A denoting the areal fraction of NWs. The value of the conductivity exponent was fixed at 1 (red curve). Green curve resulted with a fixed exponent of 1.33 but with negligible difference in goodness of fit b). The best-fit percolation threshold, 0.08, corresponded to the NW concentration of 0.087 mg/mL back-calculated using the best-fit values of a and b.

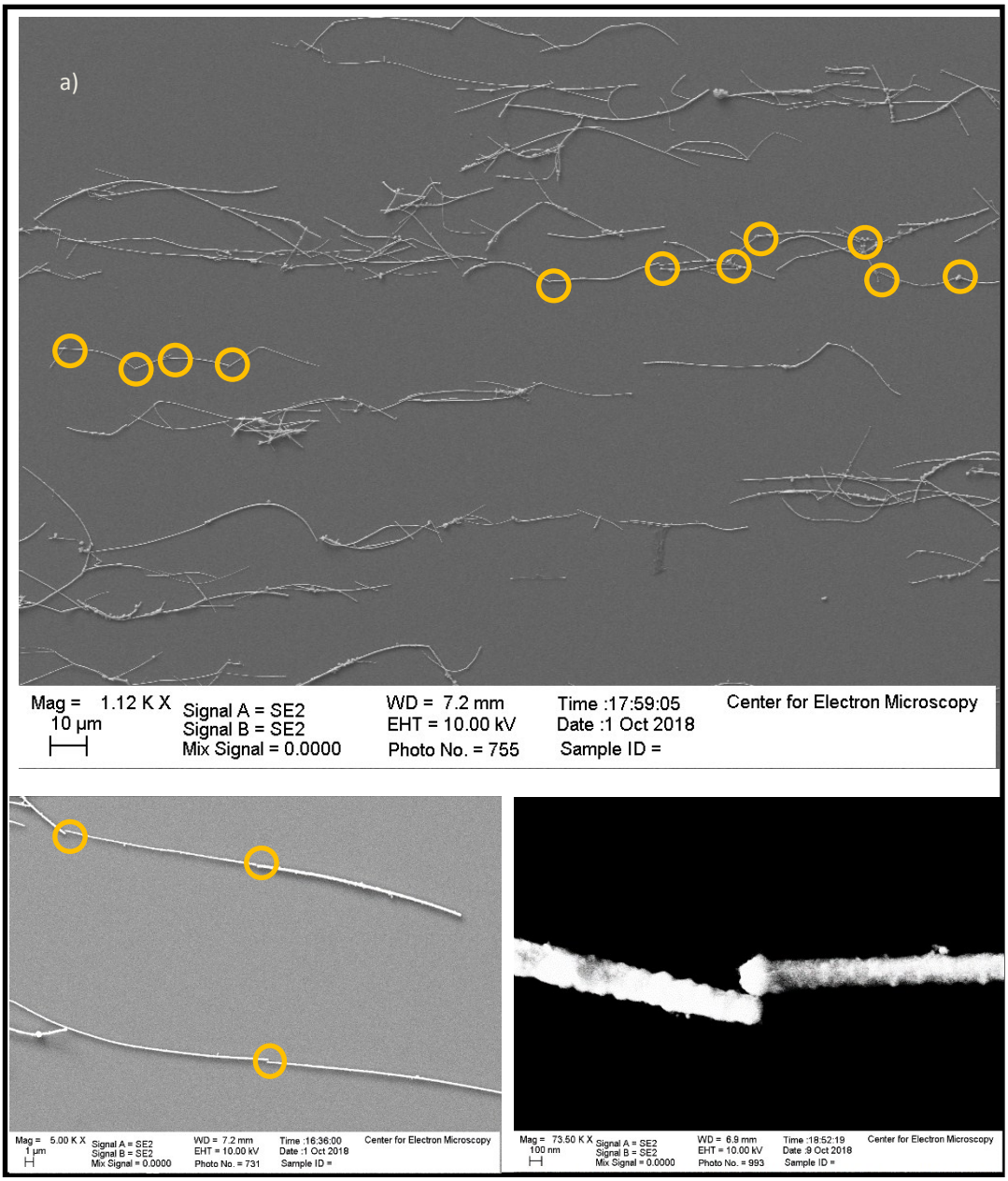

Figure S17 End-to-end contacts (indicated by yellow circles) observed at several magnifications in a magnetically aligned Cu/Ni NW suspension a). Types of end-to-end contacts observed at higher magnification; the last image is magnified image of the contact from the prior image at 100 nm scale b). The variety of contacts led us to postulate a Gaussian distribution model as described in main body of text.

A rough estimate of the average NW to NW junction resistance

Procedure for crafting single channel resistor containing nanowires: The procedure involves: a) Selective deposition of NWs into the thiol-functionalized and photolithography patterned trenches on CDO wafer and, b) fabrication of silver contact pads.

a) Selective deposition of NWs in thiol functionalized and photolithographically patterned trenches: The thiol-functionalized CDO substrate was spin-coated with positive tone photoresist (*SPR 220 3.0, Shipley*)to yield a film thickness of 3.0 ± 0.2 µm. Trench patterns (*4000 µm × 300 µm channels for self-assembly of NWs*) were transferred into the photoresist film by exposing the photoresist coated wafer to UV light (365 nm) in a benchtop projection mask aligner (*Tamarack scientific Co., Model-162*). Processing conditions are shown in a table below. Photolithography patterned substrate was placed in between the electromagnets, and 50 µl of the aqueous NWs solution (*0.5 to 2.0 mg/mL NWs solutions for self-assembly experiments and 0.1 mg/mL NWs solution was used for NW to NW junction resistance determination*) was deposited and allowed to dry on top of the substrate. The NWs deposited in the trenches bound strongly to the substrate due to covalent thiol bonds whereas the NWs deposited on photoresist were loosely bound which were removed along with photoresist by an acetone wash.

Photolithography processing steps	**Conditions**
Photoresist	SPR 220 3.0 (Shipley), Positive tone resist
Spin coating speed	3500 RPM for 4 minutes
Pre-exposure bake	110 °C for 90 Sec
UV exposure duration	5 minutes
Post-exposure bake	110 °C for 90 Sec
Developer solution	0.1M NaOH aqueous solution
Development time	40 Sec

b) Silver contact pads deposition and electrical characterization: For 4000 µm × 300 µm channels, the silver ink was deposited on both ends of the NWs self-assembled channel (visible to naked eye) using micropipette. For smaller channels, silver ink (100µL) was deposited while observing through the low magnification objective lens (10x) in an optical microscope (Olympus BX51). Silver ink was allowed dry under ambient conditions, and the electrical resistance measurements were conducted using the Keithley-615 programmable digital meter. The contact resistance between the digital multimeter probes and silver contact pads were < 1Ω, which were negligible in comparison to the resistance of the NWs channel.

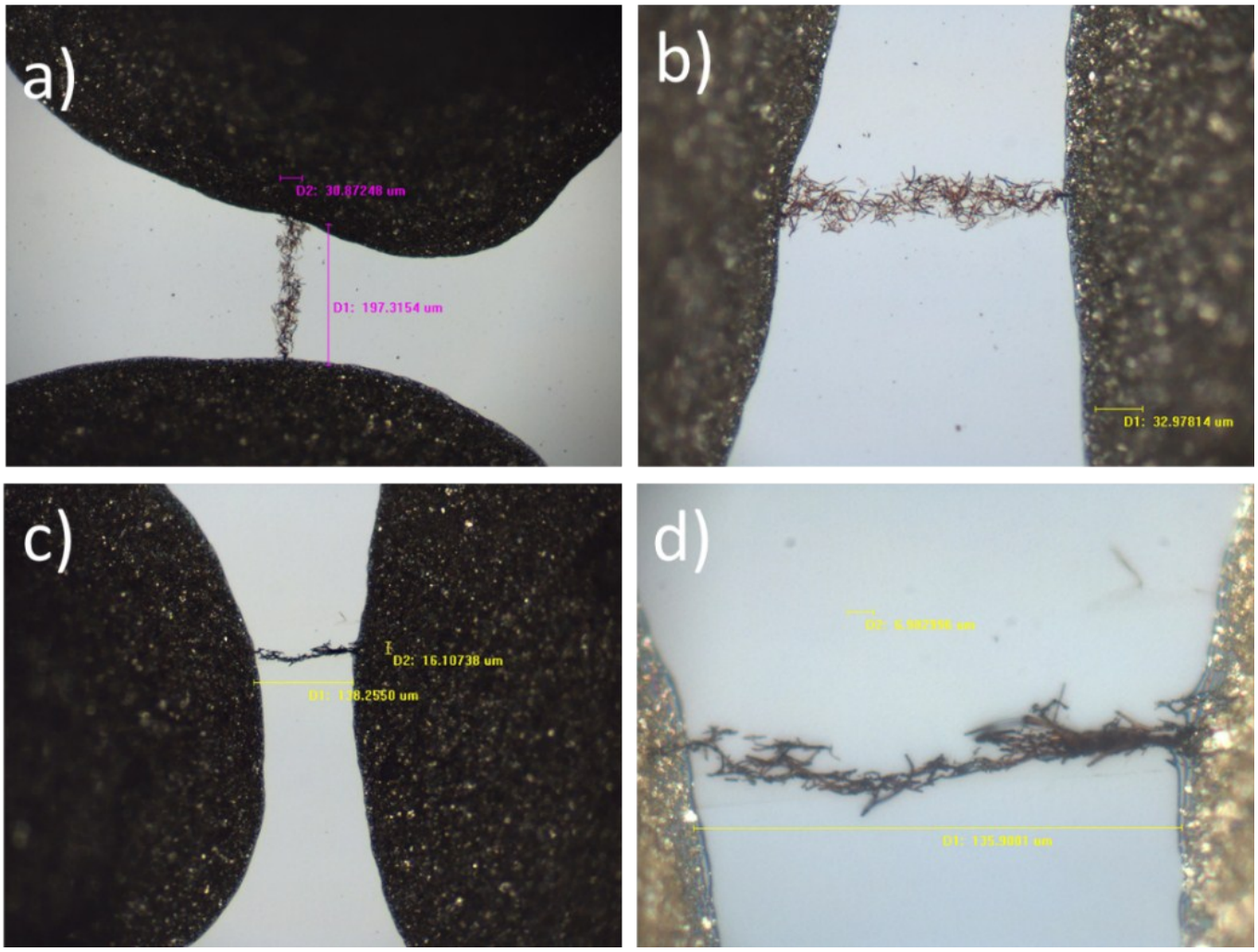

Figure S18. Images a) and b) show optical micrographs of pure Cu NWs channels (30µm × 197µm) under low and high magnification respectively. Images c), and d) show the magnetic field aligned Cu/Ni NWs (16 µm × 138 µm).

An upper limit for the NW junction resistance was evaluated by considering a small NW-cluster connecting the two electrodes. Just above the percolation limit, there should be a single macroscopic cluster that connects the two electrodes. Experimentally, in this region, it was straightforward to count the number of nanowires (*N*) in such a cluster. In the images presented above, the concentration of NWs employed to create these channels was 0.1mg/mL which was just above the percolation threshold ($C_{(percolation)}$ ≈ 0.09 mg/mL, according to data shown in Figure S16) deposited in *15-30 µm × 150-200 µm* channels, Figure S18. We assumed that the electron transport involved passage through ≈*N* NWs connected by ≈ *M* NW-NW junctions before reaching the counter electrode. In general, M>N since Cu-NW contacts were not end-to-end type; however, approximating *M = N* allowed extracting an upper limit of the $R_{Junction}$

Copper nanowires: As discussed in the main body of the text the R_{CuNW} = 145 Ω. A cluster of NWs was distributed in the channel of *30µm × 197µm* in size. Measured values of *N* and the channel resistance were 198 and 1.84 MΩ respectively.

$$R = NR_{Junction} + NR_{NW}$$

$$1840000\ \Omega = 198 * R_{Junction} + 198 * 145\ \Omega$$

$$R_{Junction} \approx 9.1\ k\Omega$$

Cu/Ni nanowires: In this case, these NWs were orientationally and positionally aligned in the magnetic field (2500 Gauss) in a *16 µm × 138 µm* size channel. The *N* and the channel resistance were 57 and 472 kΩ respectively

$$R = NR_{Junction} + NR_{NW}$$

$$472000\ \Omega = 57 * R_{Junction} + 57 * 93\ \Omega$$

$$R_{Junction} \approx 8.2\ k\Omega$$

Approximate calculation of resistance of Ni-coated copper NW ($R_{Cu/Ni}$):

Average length and diameter of Cu/Ni NWs was 15 µm and 140 nm respectively. The composite NW was assumed to be a combination of two parallel resistors:

Parallel resistance

$$\frac{1}{R(Cu/Ni)} = \frac{1}{R(cu)} + \frac{1}{R(Ni)}$$

$$\frac{1}{R(Cu/Ni)} = \frac{1}{145\ \Omega} + \frac{1}{R(Ni)}$$

$$\frac{1}{R(Cu/Ni)} = \frac{1}{145\ \Omega} + \frac{1}{257\Omega}$$

$$R_{Cu/Ni} = 93\ \Omega$$

Calculation R_{Ni} for the Ni coating on the copper NW.

$$R = \frac{\rho . L}{A}$$

$\rho_{Ni} = 6.99x10^{-8}\ \Omega.m$ at 20 °C

$L = 15x10^{-6}\ m$

Cross sectional area of nickel (Ni) coating $A = \pi r_1^2 - \pi r_2^2$

r_1 = radius of outer surface (70 nm), r_2 = radius of inner surface (60 nm)

$$= 6.99x10^{-8}\ \Omega.m.\ x\ \frac{15x10^{-6}\ m}{4.08x10^{-15}\ m^2}$$

$$= 257\ \Omega$$

More sophisticated analyses are provided by considering a percolation model of conductivity (Figure S16) and network resistance model (Figure 6b) in the main body of text.

Homogeneity of large-scale magnetic alignment and the factors affecting it

Convection and magnetic field homogeneity can in principle affect the homogeneous deposition and alignment of NWs on a large area.

Convection effect: In these studies, we did not observe effects of convection. Systematic field dependence of the deposited nanowires illustrates this observation (Figure S6) wherein we would have expected significant disruption of the aligned chains. We suggest that the convection effects are quenched owing to high thermal conductivity/diffusivity of suspended metallic nanowires. The onset of convection requires Reynold number (*Re*) to be above 1200 for a liquid with one open air-liquid interface and second solid-liquid interface as is the case here. *Re* is given as:

$$Re = \frac{\Delta T \rho_0 g \beta L^3}{\mu \alpha}$$

Where:

ρ_0 is the reference density, typically picked to be the average density of the medium,

g is the acceleration due to gravity.

is the coefficient of thermal expansion, and

ΔT is the temperature difference between solid(Si)-liquid (NW suspension) and Air-NW suspension.

L is roughly the distance separation between the two interfaces.

α is the thermal diffusivity of the system and

μ the kinematic viscosity.

L is small (-1000 µm, i.e., 100 µl drop spread over 1 cm^2. Also see below). Note, due to droplet evaporation L continuously decreases reducing the Reynold number and hence the effects of convection at later stages of droplet evaporation. *Re* can be further reduced/controlled by use of spray or spin coating techniques that can produce much thinner films. Furthermore, ΔT is likely to be smaller and α larger due to rapid heat conduction through *metallic nanowires* and the *silicon* substrate. Thus, these factors would be expected to suppress the convective flow. Nevertheless, note neither the orientational nor the positional (end-to-end positioning of NWs) ordering observed is complete implying a disordering effect of the Brownian diffusion during NW binding to the substrate

Effect of magnetic field inhomogeneity: The piling of nanowires at one edge of the glass tube (Figure 2g), and S4c) is enhanced due to *inhomogeneous* field produced by the disk-like magnets compared to the *homogeneous* field between the two opposite poles of the electromagnet of larger pole area that was used to produce alignment shown in Figure 2b. The residual weaker inhomogeneous magnetic force acting on NWs in thin liquid drops is further opposed by viscous drag forces of fluid, which would slow the migration of NWs to the drop edge. Furthermore, the NWs would also experience the gravitational sedimentation causing NW motion in the direction perpendicular to the applied external magnetic field, directed towards the high-affinity thiol-derivatized substrate. So the overall drift velocity would be directed towards the thiol-derivatized surface where they would bind irreversibly before reaching the drop edge.

Rough order of magnitude of sedimentation velocity of NWs of comparable dimension and suspended in a water-based [4]is about of 0.1-0.3 µm/sec in earth's gravitational force. The typical liquid layer thickness on the depositing surface in these studies was about 1000 um while the distance that NWs must move to reach drop edge was about five times larger, for a drop of 1cm^2. When combined with the evaporation of time of our droplets of twenty minutes, the air-liquid interface velocity (Liquid layer thickness/time of evaporation) is about 0.8 µm/s Thus, during the typical evaporation time of 20 minutes allows adequate time to an average NW to travel about 1000 µm vertically and deposit on the solid surface.

The liquid evaporation from the droplet increases in the viscosity of the liquid due to the entanglement of NWs. Irreversible chemical binding to thiol groups would provide a mechanism for uniform deposition (as it creates an additional chemical gradient that drives NWs to the solid surface). None of these effects are not present in the test tube suspension of NWs shown in Figure 2g. We expect that these factors to retard but not eliminate NWs movement to drops edge due to the residual magnetic field inhomogeneity in the laboratory electromagnet used in this study. Actual experimental data on samples collected near the edge of evaporated droplet overall 1 cm^2 area shown below exhibit imperceptible piling effect.

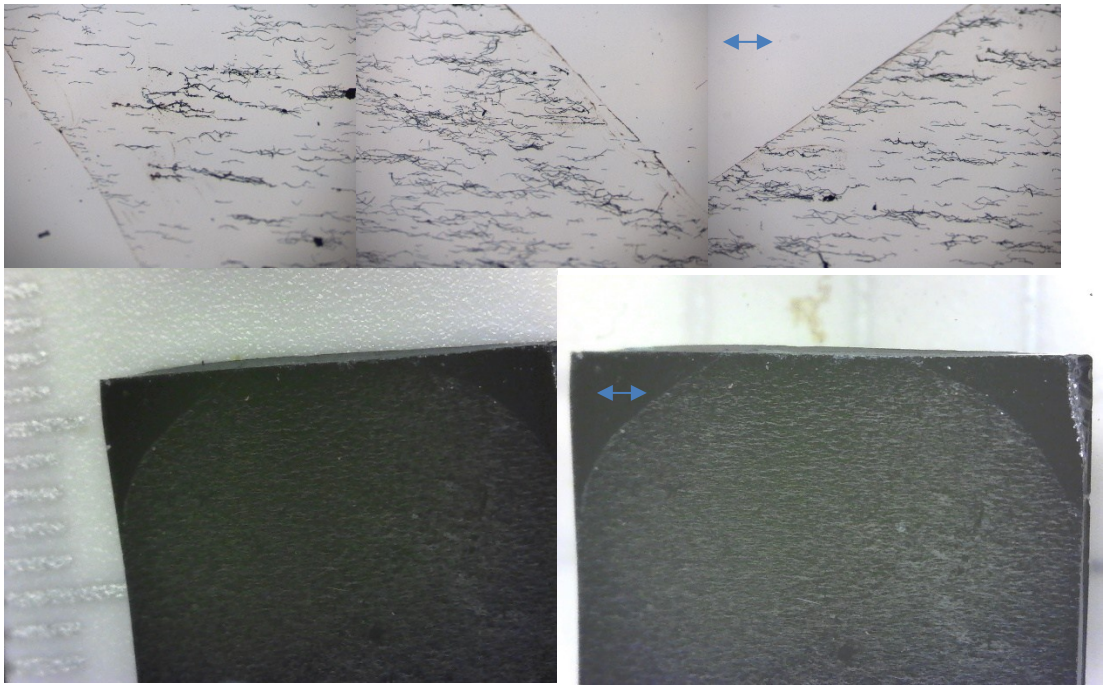

Figure S19 Macroscopic homogeneous alignment of Nanowires. Top three images show reflectance microscopic images at the three corners of drop edge. The scale bar corresponds to 100 µm and the applied H field direction is horizontal as indicated by the arrows on the scale bar. The bottom pair of images (low magnification images) are captured with a CCD camera. These images show residue of NWs deposited from droplet dried in a magnetic field (2500 G). An mm scale shown illustrates the length scale of uniform homogeneity of deposition. Please note that there is neither perceptible NW piling at the edge of droplet facing magnetic poles nor is the effect of convection rolls expected due to evaporation.

The use of MRI magnets that produce very homogeneous fields employing Helmholtz coils can further reduce piling effects

1. Hu, M.; Noda, S.; Okubo, T.; Yamaguchi, Y.; Komiyama, H., Structure and morphology of self-assembled 3-mercaptopropyltrimethoxysilane layers on silicon oxide. *Applied Surface Science* **2001,** *181* (3), 307-316.

2. Morakinyo, M. K.; Rananavare, S. B., Reducing the effects of shot noise using nanoparticles. *Journal of Materials Chemistry C* **2015,** *3* (5), 955-959.

3. Quang, D. V.; Lee, J. E.; Kim, J.-K.; Kim, Y. N.; Shao, G. N.; Kim, H. T., A gentle method to graft thiol-functional groups onto silica gel for adsorption of silver ions and immobilization of silver nanoparticles. *Powder Technology* **2013,** *235*, 221-227.

4. Chen, S.-P.; Retamal, J. D. R.; Lien, D.-H.; He, J.-H.; Liao, Y.-C., Inkjet-printed transparent nanowire thin film features for UV photodetectors. *RSC Advances* **2015,** *5* (87), 70707-70712.

TOC graphic image:

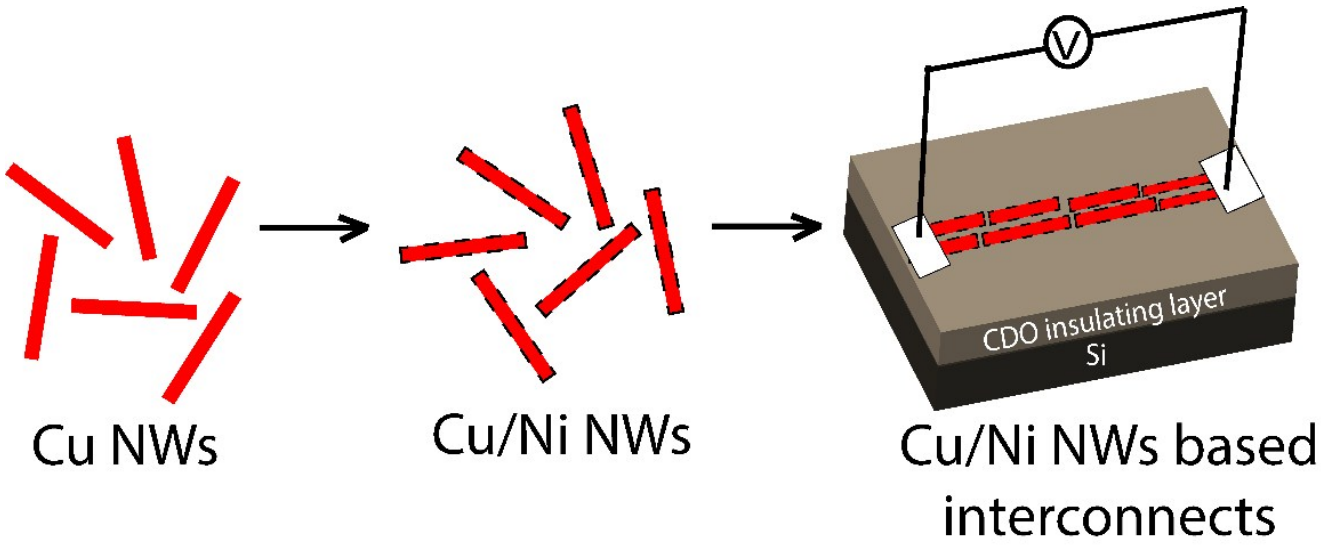

Figure. Schematic diagram showing Cu/Ni NWs based interconnect fabricated in a hybrid approach employing top-down and bottom-up methods.